PAPER

Topography on a subcellular scale modulates cellular adhesions and actin stress fiber dynamics in tumor associated fibroblasts

To cite this article: Mikheil Azatov *et al* 2017 *Phys. Biol.* **14** 065003

IOP Publishing Phys. Biol. 14 (2017) 065003 https://doi.org/10.1088/1478-3975/aa7acc

Physical Biology

PAPER

RECEIVED
12 March 2017

REVISED
13 June 2017

ACCEPTED FOR PUBLICATION
21 June 2017

PUBLISHED
3 November 2017

Topography on a subcellular scale modulates cellular adhesions and actin stress fiber dynamics in tumor associated fibroblasts

Mikheil Azatov[1], Xiaoyu Sun[2], Alexandra Suberi[2], John T Fourkas[2,3] and Arpita Upadhyaya[1,3]

[1] Department of Physics, University of Maryland, College Park, MD 20742, United States of America
[2] Department of Chemistry and Biochemistry, University of Maryland, College Park, MD 20742, United States of America
[3] Institute for Physical Science and Technology, University of Maryland, College Park, MD 20742, United States of America

E-mail: arpitau@umd.edu (A Upadhyaya)

Keywords: actin, cytoskeleton, stress fiber, focal adhesion, topography

Supplementary material for this article is available online

Abstract

Cells can sense and adapt to mechanical properties of their environment. The local geometry of the extracellular matrix, such as its topography, has been shown to modulate cell morphology, migration, and proliferation. Here we investigate the effect of micro/nanotopography on the morphology and cytoskeletal dynamics of human pancreatic tumor-associated fibroblast cells (TAFs). We use arrays of parallel nanoridges with variable spacings on a subcellular scale to investigate the response of TAFs to the topography of their environment. We find that cell shape and stress fiber organization both align along the direction of the nanoridges. Our analysis reveals a strong bimodal relationship between the degree of alignment and the spacing of the nanoridges. Furthermore, focal adhesions align along ridges and form preferentially on top of the ridges. Tracking actin stress fiber movement reveals enhanced dynamics of stress fibers on topographically patterned surfaces. We find that components of the actin cytoskeleton move preferentially along the ridges with a significantly higher velocity along the ridges than on a flat surface. Our results suggest that a complex interplay between the actin cytoskeleton and focal adhesions coordinates the cellular response to micro/nanotopography.

Introduction

The cell microenvironments in various tissues *in vivo* are composed of multiple cell types and the extracellular matrix (ECM). The ECM presents different architectures and topographies to cells, spanning length scales from nanometers to micrometers. Examples of ECM features include collagen fibrils, which can extend for tens of micrometers in length and can be as wide as 400 nm in diameter [1]. The basement membranes of cells also exhibit topographic features at nanometer scales [2, 3]. The topography of cellular environments has been found to modulate many aspects of cell function, including proliferation, polarization, differentiation, and migration [4–10]. These behaviors are indicative of the importance of topography in modulating physiological processes such as wound healing, tissue development, and cancer metastasis.

Recent advances in micro- and nano-scale fabrication techniques have enabled the mechanistic examination of cellular responses to topographic features at the sub-micron levels [11–17]. These studies have shown that cells are able to sense subtle changes in micro/nanotopography. For example, changing the dimensions of topographical features can affect cell differentiation and proliferation [18]. Nanopits and nanotubes were shown to direct the differentiation of human mesenchymal stem cells into bone-like (osteogenic) cells [19, 20]. The proliferation rates of many cell types have been shown to decrease when plated on textured surfaces [21–25], such as those with nanoscale bumps [26–28]. Finally, single cell and collective migration can also be directed along nanoridges [15, 16, 29, 30], with cells showing increased motility on these structures [31, 32]. Accompanying the more global effects of nanotopography are changes in the morphology and organization of subcellular components. Actin networks, microtubules, and focal adhesions have been found to align along the direction of nanoridges, with the degree of alignment depending on the spatial characteristics of the underlying topography [33].

These results suggest a complex interplay between intracellular components and the overall cellular sensing of topography. Most previous studies have examined static aspects of cellular and cytoskeletal organization, whereas the effect of topography on cytoskel-

etal dynamics has been confined to the phenomenon of contact guidance. The actin cytoskeletal network is the structural basis for phenomena such as cell migration, polarization, and intracellular dynamics. This network is highly dynamic and undergoes continuous reorganization, which is regulated by actin-binding proteins and motor proteins. Changes in cell morphology and dynamics are generally related to changes in actin organization and dynamics. Although signaling pathways that enable cells to sense topographical features of substrates have been of intense interest [34], as has been the movement of cells in response to nanotopography, much less attention has been paid to how cytoskeletal and intracellular dynamics respond to micro/nanotopography. In migrating *Dictyostelium*, asymmetric nano/microtopography in the form of sawtooth-shaped ridges induces actin polymerization waves in a preferred direction, which bias cell movement [16].

In this study, we investigate the effect of micro/nanotopography on the dynamics of the actin cytoskeleton in tumor-associated fibroblasts (TAFs). TAFs consist of activated fibroblasts or myofibroblasts and are found in the stroma surrounding solid tumors. Mechanisms regulating their activation and the initiation of invasion are of great interest. These cells, which are essential for promoting metastasis and invasion of cancer cells, may be particularly sensitive to the architecture and topography of the surrounding tissue in the tumor microenvironment. Furthermore, the actin crosslinking protein, palladin, is upregulated in the stromal myofibroblasts surrounding many solid tumors. Palladin is also critical in regulating cell morphology and motility. It is therefore important to understand how actin cytoskeletal organization, as regulated by palladin crosslinking, responds to micro/nanotopography of the environment. We use nanofabricated ridges of varying separation and examine the dynamics of actin stress fibers in response to alterations in groove spacing. We find that topography has a profound effect on the dynamics of actin stress fibers as well as on cell shape, actin organization, and focal adhesions. Our studies provide important insight into the modulation of cytoskeletal dynamics by topography at the subcellular scale.

Methods

Pattern fabrication and substrate preparation

Micro/nanotopographic patterns were fabricated using the multiphoton absorption polymerization (MAP) technique [35, 36]. The material used for fabrication of the surfaces is polyacrylate. We used 49 wt% SR368 (Sartomer), 49 wt% SR499 (Sartomer), and 2 wt% of Lucirin TPO-L as the formulation for surface fabrication. Both SR368 and SR499 are acrylic monomers. Lucirin TPO-L is the photoinitiator. The polymer should be benign to cells after being soaked in ethanol for several hours. This technique enabled creation of patterned surfaces with adjustable height, width, and spacing of patterns with the advantage that the refractive index of the material is compatible with total internal reflection fluorescence (TIRF) microscopy. The patterns consisted of arrays of evenly spaced, 300 μm long nanoridges (figure 1(a)). The spacing between adjacent ridges was varied between 0.8 μm and 10 μm, while the widths and the heights of the ridges were ~250 nm and ~600 nm, respectively. The polymer used for fabrication is less rigid than glass, with a Young's modulus of ~0.5 GPa [37], but it is rigid enough to maintain its shape under cell exerted forces, since cells typically deform substrates of stiffness up to 100 s of kPa.

The fabricated nanoridge surfaces were soaked in 70% ethanol for several hours to let the potentially toxic unreacted photoinitiator and byproducts diffuse out. The unreacted acrylate groups on the polymer surface can react with the amine groups on proteins through Michael addition, which facilitates the subsequent surface functionalization with fibronectin. Soaking in ethanol also served to sterilize the surfaces against bacterial growth. This procedure does not kill mold spores. However this is not necessary for our experiments, as we did not use the nanofabricated surfaces for long-term cell culture, only for imaging experiments lasting 3–4 h. Nanofabricated surfaces were discarded after being used for an imaging experiment. Surfaces were rinsed with PBS three times following ethanol treatment and were stored dry before being coated with fibronectin.

The glass coverslip with nanoridges was glued to the bottom surface of a dish with a circular hole (Mattek Corporation, Ashland, MA). Nanoridges were coated with fibronectin (from bovine plasma, Sigma-Aldrich) by first immersing them in a poly-L-Lysine solution and then incubating with 500 μl of 10 μg ml^{-1} fibronectin solution for 2 h at room temperature. We have previously shown that the fibronectin coating on these surfaces is uniform [16].

Cell culture and transfection

Tumor-associated fibroblast (TAF) cells were stably transfected with EGFP-palladin. Briefly, EGFP-palladin fragment was ligated into Z4-MSCV-mEos2-actin (a gift from Morgan Huse, Rockefeller University, New York, NY). Retroviruses were generated according to manufacturer's protocol, with Phoenix Amphotropic cells and transduced into TAFs. The cells were then selected in 100 μg ml^{-1} zeocin for 2 weeks and sorted with fluorescence-activated cell sorting to obtain fluorescent cells. Palladin showed a 2× overexpression in EGFP-palladin cells compared to WT cells based on quantitative Western blot (data not shown). EGFP-palladin labeled TAF cells were cultured at 37 °C and 5% CO_2 in Dulbecco's modified Eagle's medium (DMEM) with 10% fetal bovine serum (FBS), 1% penicillin-streptomycin, and 1% sodium pyruvate (Life technologies, Grand Island, NY). For static measurements and stress fiber tracking experiments, cells were plated on nanoridges 3 h prior to the experiment. Imaging medium L-15 (Life technologies, Grand Island, NY) was used for microscopy.

Immunostaining

Cells were plated on substrates of interest and allowed to spread for 3 h, then fixed with 4% paraformaldehyde (PFA) solution for 7 min, washed with phosphate buffered saline (PBS), and permeabilized with 0.2% solution of Triton-X for 2 min. They were then washed with PBS and blocked (2% BSA in PBS) for 1 h. Cells were incubated with primary antibody (monoclonal mouse paxillin B-2, Santa Cruz Biotechnology) in blocking solution for 1 h, washed in PBS and incubated in secondary antibody solution (Alexa Fluor 546 goat anti-mouse IgG2b, Invitrogen) for 1 h in the dark.

Live-cell microscopy

Fluorescence and interference reflection microscopy (IRM) images were collected at 37 °C using an inverted microscope (TE2000 PFS, Nikon, Melville, NY) with a 60×, 1.49 NA objective lens. The signal was collected from a cooled CCD camera (Coolsnap HQ2, Photometrics, Tucson, AZ) using Andor iQ acquisition software. A halogen lamp was used for bright-field imaging. A mercury lamp with appropriate filters was used to provide the 488 nm light to excite the palladin for wide-field imaging. TIRF imaging was performed using a 491 nm laser (100 mW, Andor, South Windsor, CT) and a 561 nm laser (75 mW, Andor). For stress fiber tracking, cells were imaged every 20 s in wide-field fluorescence mode. For spreading experiments, cells were imaged every 20 s in TIRF mode.

Analysis of cell shape and orientation

We used IRM or bright-field imaging to visualize the nanoridges and wide-field fluorescence imaging to define the outline of the cell edge. Images were analyzed using automated MATLAB software. The built-in edge-detection tool in MATLAB was applied to the cell fluorescence images. Detected edge pieces were connected by dilating the image, filling in the holes in the cell boundary, and finally eroding the image back to its original edge (because dilation advances the boundary of the cell). The identified cell outlines were analyzed for area, orientation and eccentricity. Each outline was fit to an ellipse to quantify the alignment of the cell with respect to the direction of the nanoridges (defined as the angle between the major axis and direction of ridges) and the cell elongation index (defined as the ratio of the major and minor axes of the ellipse). The direction and location of ridges were found by applying a band-pass filter to a bright-field image.

In all the box plots shown, the red horizontal line shows the median of the data, the box represents the lower (first) and upper (third) quartiles of the data, while the maximum whisker length is set to be 1.5 times the inter-quartile range (IQR). The data outside the whiskers (outliers) are shown with red crosses. To test statistical significance we used a non-parametric Wilcoxon rank sum test for two independent data sets to test for the equality of population medians. This test is used for populations that cannot be assumed to be normally distributed.

Analysis of stress fibers and focal adhesions

To identify stress fibers, we applied a band-pass filter to minimize the interference of noise and low-frequency background fluorescence, and then converted to a binary image. Using MATLAB's regionprops function, we identified segments of stress fibers along with their approximate direction. We applied a direction-specific closing algorithm to better connect the identified stress fibers without the merging of parallel stress fibers while connecting segments from the same fiber. Stress fiber orientation (SFO) was measured as a weighted average of cosines of the angles of each individual stress fiber, with respect to the angle between individual stress fibers and the nanoridges (α). The average is weighted by stress fiber length.

$$\mathrm{SFO} = \frac{\sum \mathrm{Length(SF)} \cdot \cos\alpha}{\sum \mathrm{Length(SF)}}, \qquad (1)$$

where Length(SF) is length of the stress fiber. For a large number of randomly distributed stress fibers, $\mathrm{SFO_r} = \frac{\int_0^{\pi/2} \cos x \mathrm{d}x}{\pi/2} = \frac{2}{\pi} \approx 0.64$. Similarly, the stress fiber order parameter (SFOP) is defined as a weighted average of cosines of the angles of each individual stress fiber (γ) with respect to the average direction of stress fibers (β). The average angle, β, is the weighted average direction of stress fibers

$$\mathrm{SFOP} = \frac{\sum \mathrm{Length(SF)} \cdot \cos(\beta - \gamma)}{\sum \mathrm{Length(SF)}}. \qquad (2)$$

For a large number of randomly distributed stress fibers, $\mathrm{SFOP_r} = \frac{\int_0^{\pi/4} \cos x \mathrm{d}x}{\pi/4} = \frac{2\sqrt{2}}{\pi} \approx 0.9$, whereas the minimum value of SFOP would be for the cells with only two perpendicularly oriented stress fibers, which would result in $\mathrm{SFOP_m} = \cos\frac{\pi}{4} \approx 0.71$.

We analyzed focal adhesions using ImageJ by drawing a polygon around each visually identified focal adhesion and fitting an ellipse around each polygon. The length and orientation of each focal adhesion as a length and orientation of ellipse's major axis were then calculated. We compared the fluorescent image with IRM and bright-field images to determine whether each individual focal adhesion was located on a ridge.

Tracking and analysis of palladin bands

The actin crosslinker palladin is a component of actin stress fibers and forms distinct bands (puncta) along the length of the fibers. These puncta act as markers for the dynamics of the actin stress fibers and provide us with a unique tool to track and analyze the response of the actin cytoskeleton in the cell. Although myosin also localizes to stress fibers in a similar pattern, our transient transfections with RFP-myosin did not have

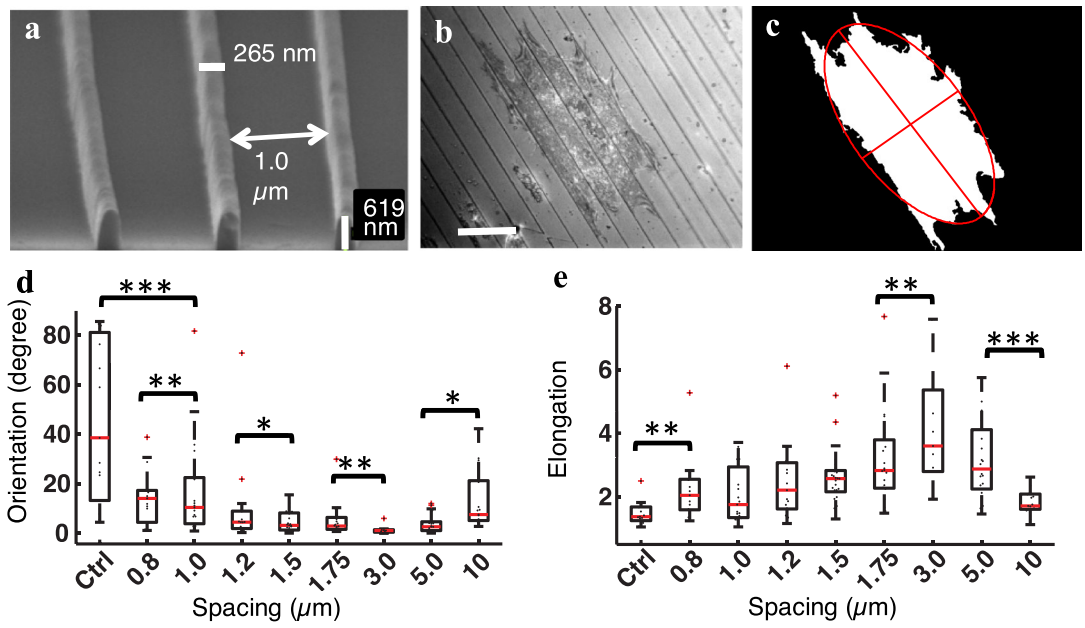

Figure 1. Cell shape and orientation are modulated by topography. (a) Scanning electron micrograph (SEM) of nanoridges. Each nanoridge has a width of ~250 nm and a height of ~600 nm. The spacing shown is 1 μm. (b) IRM image of a cell on nanoridges with a 10 μm spacing after spreading for ~3 h. The black diagonal lines correspond to the tops of the nanoridges. Scale bar: 20 μm. (c) Representative output of the cell analysis software. The white region is the detected outline of the cell. In red is the best fit ellipse around the cell, with its major and minor axis. (d) Comparison of the angle of the cell body with respect to the direction of the nanoridges. (e) Ratio of the length of two axes of the fit ellipse showing the relative elongation of the cell with respect to the spacing of the surface. The quantified parameters on all patterned surfaces were statistically different from the flat control ($p < 0.05$). Statistical significance was determined using the Wilcoxon test. Fifteen to twenty cells were analyzed for each nanoridge spacing. ($^{*}P < 0.05$, $^{**}P < 0.01$, $^{***}P < 0.001$; Wilcoxon rank sum test.)

a sufficiently high signal-to-noise ratio for robust tracking.

Positions of palladin spots were corrected for drift by tracking immobile structures in the IRM image and computing the mean displacement of those structures for every frame. The tracking algorithm consisted of two main parts: spot identification for every frame and combining spots into tracks. The final version of the software was created by combining the spot detection algorithm [38] and a tracking algorithm (http://site.physics.georgetown.edu/matlab/). The spot identification algorithm allows us to vary the minimum spot brightness of detected spots so that we can control the quality of located spots. After the spot locations are determined, the algorithm uses a center-of-mass calculation in the pixels around the maximum to measure the coordinates of the spot with sub-pixel accuracy.

To quantify the directionality of the tracks, we defined two angles, θ and φ, with respect to the direction of the ridges and with the previous displacement, respectively.

$$\theta(t, \Delta t) = \text{angle}([\vec{r}(t+\Delta t) - \vec{r}(t)], \vec{d}) \quad (3)$$

where $\vec{d}$ is the direction of the ridges, $\varphi(t, \Delta t) = \text{angle}(\vec{r}_1, \vec{r}_2)$ and $\vec{r}_1 = \vec{r}(t) - \vec{r}(t+\Delta t)$ and $\vec{r}_2 = \vec{r}(t+\Delta t) - \vec{r}(t)$.

For each track we computed the mean-squared displacement (MSD), which is defined as

$$\langle \Delta r^2(\Delta t) \rangle = \langle (\vec{r}(t+\Delta t) - \vec{r}(t))^2 \rangle \quad (4)$$

where $\vec{r}(t)$ is the current position of the spot and Δt is the time lag. The brackets indicate the time average for each particular track. Each MSD was fit to

$$\langle \Delta r^2(\Delta t) \rangle = c + D\left(\frac{\Delta t}{t_0}\right)^{\beta} \quad (5)$$

where $t_0 = 1$ without loss of generality and c, D, and β, are fit parameters. As seen from equation (5), as $\Delta t \to 0$, $\langle \Delta r^2(\Delta t) \rangle \to c$, while for long times, $\langle \Delta r^2(\Delta t) \rangle \to D\left(\frac{\Delta t}{t}\right)^{\beta}$.

Artifactual particle motion may arise from phenomena such as stage vibrations, temperature fluctuations, and photon counting noise. We performed control experiments to quantify the amount of noise in our apparatus and analysis. We plated immobile beads on the same substrates, imaged them under similar conditions, and performed the same analysis. Even though the beads were immobile, the tracking algorithm found different coordinates for each frame, leading to different velocities and turning angles. Comparing results for different substrates with the results for noise (supplementary figure 1) (stacks.iop.org/PhysBio/14/065003/mmedia), we find that (1) the noise turning angle distribution has only one peak around 180°, as expected for a constrained particle and (2) noise velocities are lower than velocities of palladin bands within cells, indicating that our tracking algorithm is able to detect band movements with high signal-to-noise ratios [16].

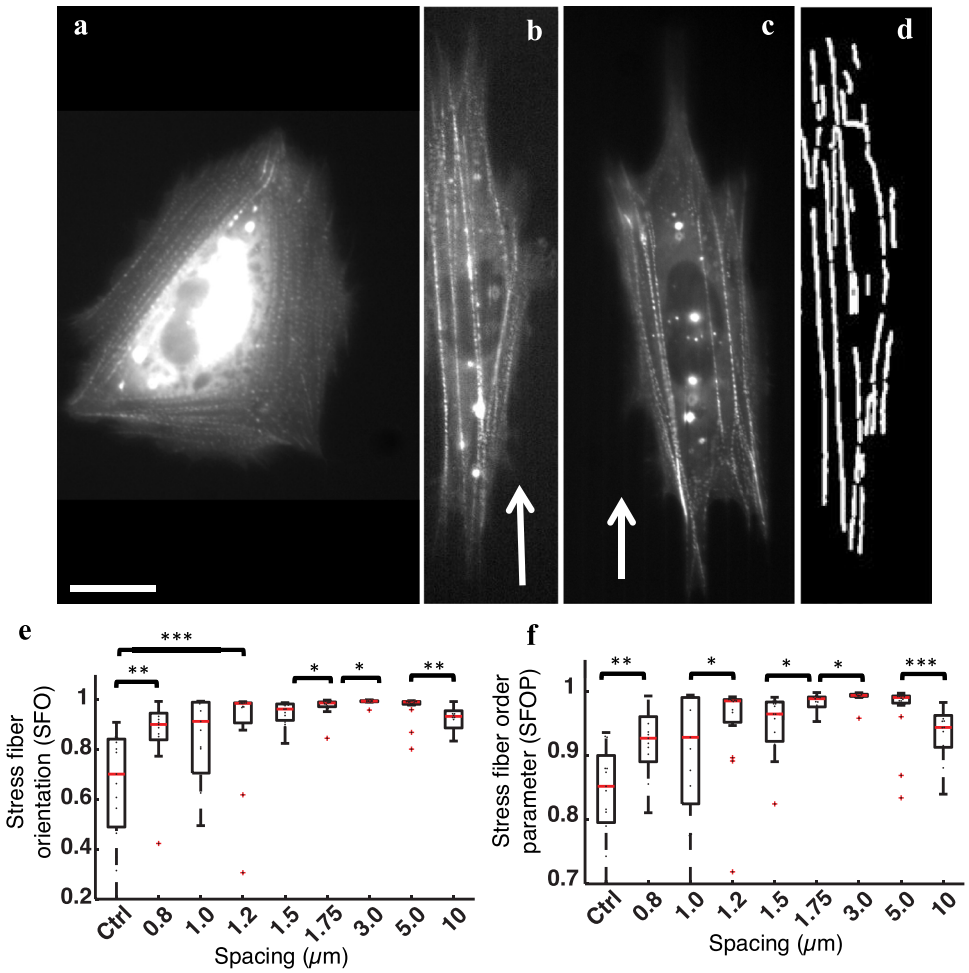

Figure 2. Micro/nanotopography modulates the organization of stress fibers. Widefield fluorescence image of an EGFP-palladin-expressing cell spead on (a) a flat surface, (b) nanoridges with a 3 μm spacing, and (c) nanoridges with a 5 μm spacing. Scale bar: 20 μm. The arrows point along the direction of the ridges. (d) Processed image of the cell after analysis. White lines show the stress fibers detected in the image in (b). From the length and direction of each individual stress fiber we determine the overall stress fiber orientation and order parameter. (e) Comparison of SFO on patterns with spacings ranging from 0.8 μm to 10 μm (as indicated on the x axis). Stress fibers are more aligned on patterned surfaces. The degree of alignment peaks at a spacing of 3 μm. (f) Stress fiber orientation order parameter (SFOP) with respect to the spacing of the patterns. Stress fibers are aligned with ridges for all spacings, with the degree of alignment peaking for a spacing of 3 μm. On all patterned surfaces the degree of alignment was statistically different from that on a flat control. Fifteen to twenty cells were analyzed for each patterned surface used. ($^{*}P < 0.05$, $^{**}P < 0.01$, $^{***}P < 0.001$; Wilcoxon rank sum test.)

Results

Cell elongation and alignment are sensitive to micro/nanotopography

We nanofabricated surfaces that had parallel ridges with variable spacing, with the ridge being ~265 nm wide and ~600 nm high (figure 1(a)). We first quantified how tumor associated fibroblasts (TAF) responded to patterns of different sizes by analyzing the alignment of cell shape for ridge spacings ranging from 0.8 μm to 10 μm. We allowed TAF expressing EGFP-palladin to spread fully on patterns with different spacings for ~3 h and analyzed the cell area, elongation and orientation of the cell body (as defined in Methods) for different ridge spacings (figures 1(b) and (c)). Cells on all patterned surfaces examined exhibited a strong alignment with the direction of the nanoridges (figure 1(d)), with the median alignment angle (see methods) within 10° of the direction of the ridges and maximal at 3 μm ridge spacing. Cells also exhibited more elongated shapes on the ridges, with the median elongation index being maximal for surfaces with 3 μm spacing and nearly 4 times as elongated as those on flat surfaces (figure 1(e)).

Stress fiber orientation is modulated by micro/nanotopography

We next examined the response of cytoskeletal organization to micro/nanotopography using TAFs expressing the actin-binding protein, EGFP-palladin, which preferentially labels actin stress fibers [39]. In fully spread cells, palladin clearly assembled onto actin stress fibers that spanned the entire cell and ran along the edges of the cell, often determining the cell's shape and orientation (figures 2(a)–(c)). We used custom software to identify stress fibers from fluorescence images (figure 2(d)), as described in Methods. We found that stress fibers at the cell edges and in the interior of the cell were generally aligned with the direction of

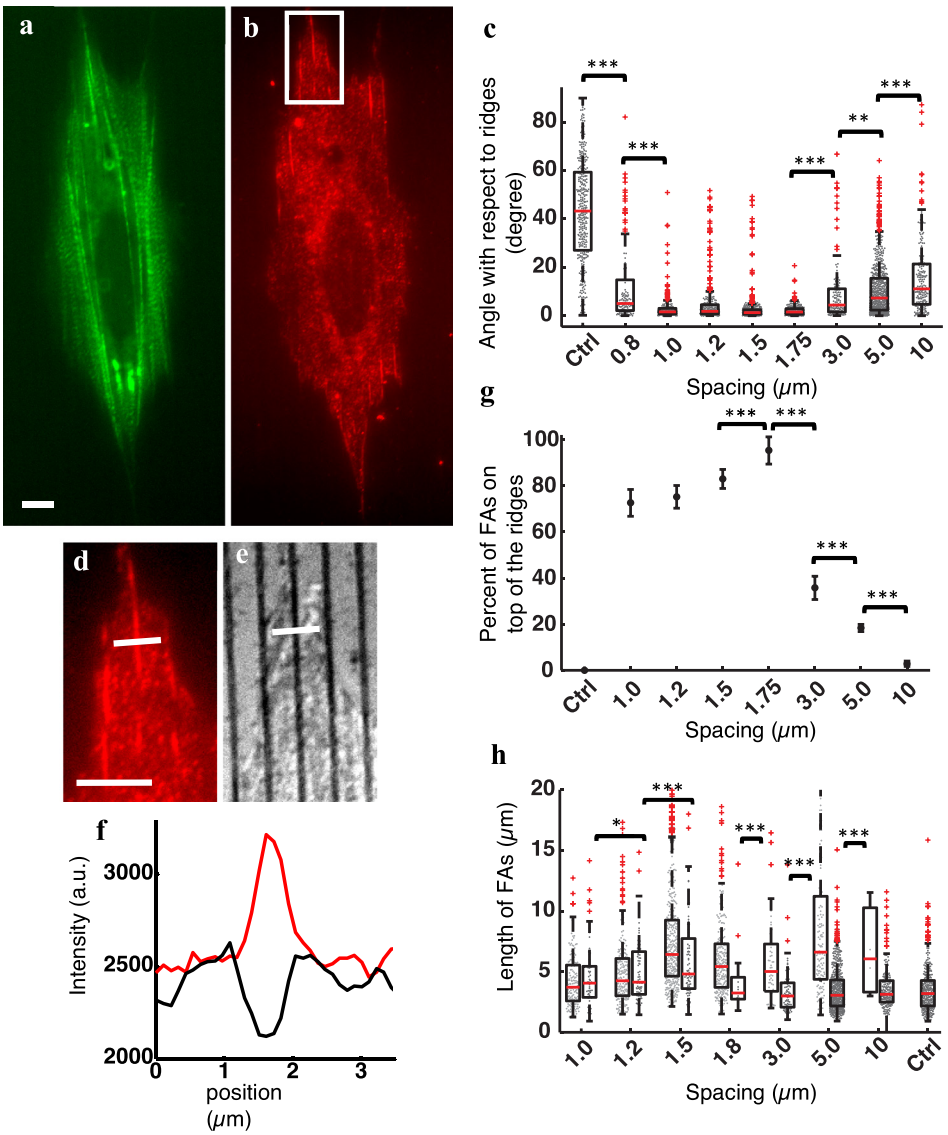

Figure 3. Focal adhesions align with micro/nanopatterns and assemble on top of ridges. (a) Wide-field fluorescence image of an EGFP-palladin-expressing cell on ridges with 3 μm spacing after 3 h of spreading, fixing, and immunostaining of paxillin. Scale bar: 5 μm. (b) TIRF image of paxillin showing localization of focal adhesions. (c) Distribution of angles of focal adhesions with respect to type of surface used. All patterned surfaces were significantly different from the flat surface (Ctrl). Statistical significance was determined using the Wilcoxon test. (d) TIRF image of paxillin obtained from the white box in panel B. Scale bar: 5 μm. (e) IRM image of the region in panel C showing locations of the ridges. (f) Intensity profile along the white line in panels (d) and (e), perpendicular to the ridges. The red line profile corresponds to paxillin intensity and the black line profile corresponds to the IRM image intensity. The peak of the red line, which corresponds to focal adhesions, correlates with the trough of the black line, which corresponds to the ridge. These types of focal adhesions are considered to be on top of the ridges. (g) Percent of focal adhesions on top of the ridges as a function of the spacing. Statistical significances were determined using the Fischer's exact test ($p < 0.001$). (h) Distribution of focal adhesion lengths for different ridge spacings. Two bars correspond to each spacing. (left) Light gray bar corresponds to the tops of the nanoridges. (right) Dark gray bar corresponds to the bottoms of the nanoridges. The flat surface (ctrl) has a single bar. Statistical significances were determined using the Wilcoxon test. For statistical analysis, ten to twenty cells, totaling 200–600 focal adhesions, were used for each spacing. ($^{*}p < 0.05$, $^{**}p < 0.01$, $^{***}p < 0.001$; Wilcoxon rank sum test.)

ridges for all spacings. While stress fibers were oriented at a variety of angles for any given surface, the degree of alignment was higher on ridged surfaces compared to a flat surface. This was quantified and observed as significant differences in the stress fiber orientation and the stress fiber order parameter between each patterned surface and a flat surface. Stress fiber orientation (SFO, equation (1)) exhibited a biphasic behavior as a function of the ridge spacing (figure 2(e)), with the degree of alignment maximal at 3 μm, consistent with the finding that cells were maximally elongated for ridges with 3 μm spacing. The SFO on flat surfaces was not significantly different from SFO_r, the value of the SFO for randomly distributed stress fibers (see Methods). Similarly, the order parameter (SFOP, equation (2)) showed a biphasic dependence on ridge spacing (figure 2(f)). SFOP for cells on flat surfaces was between $SFOP_r$ and $SFOP_m$, the value of SFOP for large number of randomly distributed stress fibers and the minimum possible value of SFOP, respectively (See methods). These results are in agreement with the cell-shape alignment results, and suggest that stress fiber alignment is important in the overall micro/nanotopographical mechanosensing of cells.

Focal adhesions guide cell alignment on micro/nanoridges

Because many stress fibers in cells originate from focal adhesions, it is likely that focal adhesions serve to align stress fibers as they are generated. Some previous studies have found that focal adhesions are aligned in the direction of ridges [15, 33], which suggests that they may play an important role in the sensing of nanotopography. However, most previous studies have reported qualitative observations of focal adhesions on topographically patterned surfaces (but see [40]). We examined the organization of focal adhesions in TAF cells to further test these ideas.

To quantify focal adhesions, we fixed EGFP-palladin-expressing TAFs after 3 h of spreading on different surfaces and stained for paxillin, a focal adhesion marker. We visualized focal adhesions by TIRF microscopy using both palladin (green) and paxillin (red) (figures 3(a) and (b)). Focal adhesions were strikingly aligned with nanoridges on all surfaces. Analysis of the angular distribution of focal adhesions (from the paxillin images) with respect to ridges showed that these angles were small, with a median $<10°$, for all surfaces with ridges. The angles exhibited a biphasic dependence, with the smallest angles being found for substrates with spacing between 1.0 and 1.75 μm (figure 3(c)). Comparison of fluorescence and IRM images (figures 3(d)–(f)) showed that focal adhesions were most likely to form on the tops of the ridges and that the percentage of focal adhesions on top of the ridges varied strongly with ridge spacing (also see [44]). Although most focal adhesions formed on the tops of the ridges for surfaces with smaller spacings, the percentage of focal adhesions growing on top declined rapidly for substrates with 3 μm and 5 μm spacings, with almost none growing on top of ridges for surfaces with a 10 μm spacing (figure 3(g)). Because focal adhesions are most likely to form on top of ridges, we observed few focal adhesions with large angles on surfaces with ridge spacings in the range from 1.0 to 1.75 μm. For larger nanoridge spacings, focal adhesions could form between the ridges, resulting in a larger range of angles. We also found that focal adhesions on top of ridges were longer compared to those in grooves, which were similar in length to focal adhesions on flat surfaces (~3.5 μm) (figure 3(h)). Thus, focal adhesions matured preferentially and to significantly greater lengths on top of ridges (they could be almost twice as long, ~6.6 μm, on ridges with 5 μm spacing). These results indicate that focal adhesions are sensitive to the micro/nanotopography of their environment.

Micro/nanotopography modulates stress fiber dynamics

Although the above findings indicate that micro/nanotopography modulates cell shape, stress fiber orientation, and adhesion formation, little is known about how topography at this scale affects cytoskeletal dynamics. While micro/nanotopography was shown to modulate actin waves in migrating cells [16], its effect on the dynamics of stress fibers is unknown. Previous work has studied movements of external particles and beads embedded in the cell, over time scales in the range of milliseconds to seconds [41–43]. However, cytoskeletal dynamics also occur over longer time scales. For instance, actin bundles in the cell reorganize over time scales of minutes to hours [44].

To study these dynamics, we took advantage of the observation that EGFP-palladin localized as punctate bands on stress fibers (as shown on a patterned and flat surface, respectively, in figures 4(a) and (d)). Because palladin puncta could be identified and tracked with a high signal-to-noise ratio (figures 4(b), (c) and (e)) as described in Methods, we exploited this feature to quantify the dynamics of stress fibers. Tracking these bands yields a measure of the stress fiber and cytoskeletal dynamics without relying on externally introduced particles attached to the cytoskeleton. Shorter tracks in figure 4(e) show that the actin cytoskeleton dynamics are slower on a flat surface than on the patterned surface in figure 4(c).

Figure 4(f) shows a typical measured track of a palladin band on a stress fiber. To quantify the stress fiber directionality, we defined two angles, one between the instantaneous velocity of the track and the direction of the ridges (θ) and another with the previous displacement (φ) (see methods for more details). Although the distribution of θ indicates the alignment of the track with respect to the ridges, the distribution of φ represents the directional persistence of the track. The distribution of $\theta(t, \Delta t)$ was peaked for all patterned surfaces (figure 4(g)), whereas the distribution on a flat surface was uniform (figure 4(h)). Gaussian fits to the angle distributions on patterned surfaces peaked at ~0°, indicating that palladin bands were more likely to move parallel to the ridges. The width, or standard deviation, of the Gaussian function indicates the overall preference to move in the direction of the ridges. The standard deviation decreased for larger time steps, indicating that the motion was more likely to be along the ridges over long time scales (figure 4(i)). Furthermore, surfaces with 1 μm and 10 μm spacings had the largest standard deviations, whereas surfaces with 3 μm spacing had the smallest, indicating that palladin tracks have the greatest probability of moving along ridges that are separated by 3 μm. Because we observed directional bias on both short and long time scales, these results hint that micro/nanoscale features of topography potentially modulate the direction of movement of the actin cytoskeleton directly, by decreasing the probability of individual palladin bands moving orthogonally to the ridges.

We next examined how micro/nanotopography modulated the magnitudes of the velocities of palladin bands. The distribution of instantaneous speeds of tracked bands exhibited a peak at about 3 nm s^{-1} for both flat and ridged surfaces, with a more extended tail than a Maxwellian distribution, as would be expected for an equilibrium process. The

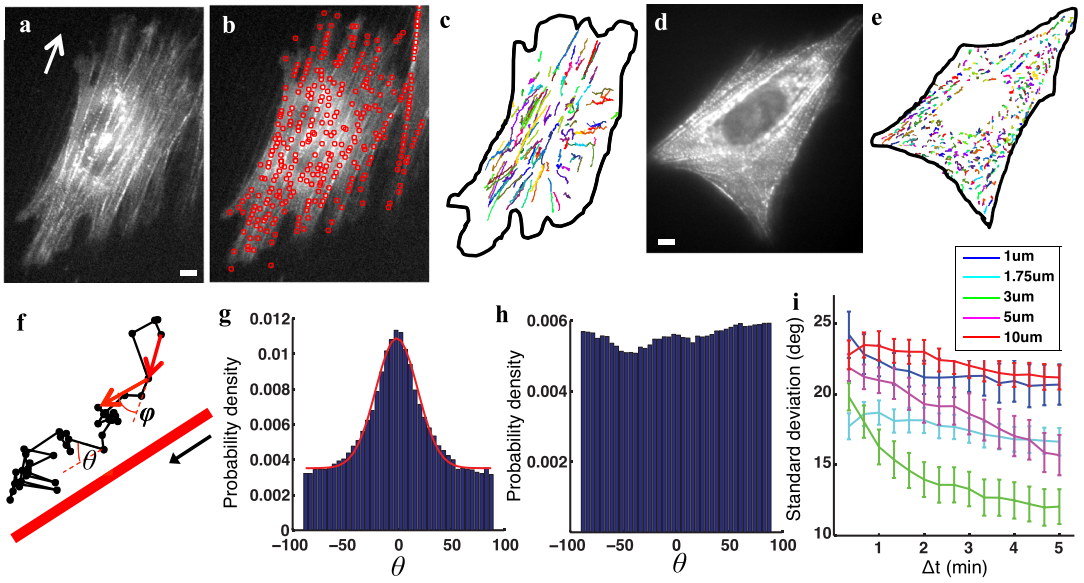

Figure 4. Stress-fiber dynamics are modulated by surface topography. (a) Wide-field fluorescence image of an EGFP-palladin-expressing cell on nanoridges with a 3 μm spacing. The arrow in the upper left corner shows the direction of the nanoridges. Scale bar: 5 μm. (b) Example of spot detection for an image of a cell spread on nanoridges with a 3 μm spacing. The red circles indicate the positions of each palladin band. (c) Examples of palladin tracks superimposed on the outline of the cell in (a). (d) Wide-field fluorescence image of EGFP-palladin cell on a flat surface. Scale bar: 5 μm. (e) Examples of palladin tracks superimposed on the outline of the cell in (e). (f) An example of the trajectory of one of the palladin bands obtained from a cell on a surface with 5 μm spacing. This illustrates the definitions of $\theta(t,\Delta t)$, $\varphi(t,\Delta t)$, $\vec{d}$, $\vec{r}_1$, and $\vec{r}_2$, (g) distribution of all angles $\theta(t,\Delta t)$, for $\Delta t = 20$ s, on nanoridges with a 3 μm spacing. The distribution of $\theta(t,\Delta t)$, for all cells and all Δt, fits closely to a Gaussian distribution with a y offset, and an average around 0. The red line illustrates the fit of a Gaussian function to the angle distribution. (h) The distribution of angles for a flat surface showing that tracks do not have a preferred direction of motion on flat surfaces. (i) Standard deviation of the Gaussian fit in degrees as a function of pattern spacing and Δt. Each color represents a different spacing, and the x-axis represents the time lag Δt.

distribution for nanoridge surfaces had a more extended tail as compared to that for a flat surface as well (as shown in figure 5(a) for a 3 μm spacing). The peak velocity on the patterned surfaces was at a slightly higher value than that on a flat surface. Cumulative velocity distribution plots (figure 5(b)), showed that instantaneous velocities have a biphasic dependence on ridge spacing, with the largest magnitudes on patterns with 3 μm spacing, which is similar to the behavior of parameters such as cell elongation and orientation, as well as stress fiber orientation. These observations are in contrast with previous studies showing that topography-induced contact guidance in *Dictyostelium* is more preferentially aligned with the groove direction for a smaller spacing [13]. We further examined whether there was a dependence of the instantaneous speeds on the direction of motion. We divided the range of possible directions ($-90°$ to $90°$) into $5°$ bins, averaged all instantaneous speeds in a given bin and plotted the resulting average speeds as a function of angle (figure 5(c)). The velocity distributions on all patterns appeared to be Gaussian, peaking at ~$0°$. This result indicates that tracks are more likely to make larger steps in the direction of ridges and smaller steps perpendicular to ridges. Thus, palladin bands are not just more likely to move in the direction of the ridges, but they do so with a higher velocity than in orthogonal directions. The height of the distribution again showed a biphasic relationship, being greatest for ridges with a 3 μm spacing (figure 5(d)). Surfaces with 3 μm spacing show the most strongly peaked velocity distribution, indicating enhanced stress fiber dynamics.

Micro/Nanotopography modulates mean-square displacement of palladin bands

Mean-squared displacement analysis of the ensemble of tracks (100–500 tracks) of palladin bands throughout the cell, with a minimum of 30 frames (15 min) for each track, showed that the motion of the bands was superdiffusive, with the power-law exponent, β, greater than 1 for all surfaces (figure 6(a)). The fit parameter, D, which is an effective diffusion coefficient, was larger for all nanoridge spacings below 10 μm than on a flat surface, with the 3 μm spacing exhibiting the largest D. Fitting individual tracks with equation (5) showed that over 94% of all tracks exhibited superdiffusive motion ($\beta > 1$), with R^2 values for the fit greater than 0.9. On closer examination of the MSD plots, we observed that the movement of bands switched from subdiffusive motion (slope less than 1) in the first few time intervals, to superdiffusive motion over longer times, as indicated by a change in slope from short time scales to long time scales seen in the MSD plots. As stated in Methods, we found that as $\Delta t \to 0$, $\langle \Delta r^2(\Delta t) \rangle \to c$ and the slope approached 0, while for large times the slope approached β. The time lag Δt_1 , or which the slope is equal to one is the point where the MSD switches from sub-diffusive to super-diffusive behavior. This

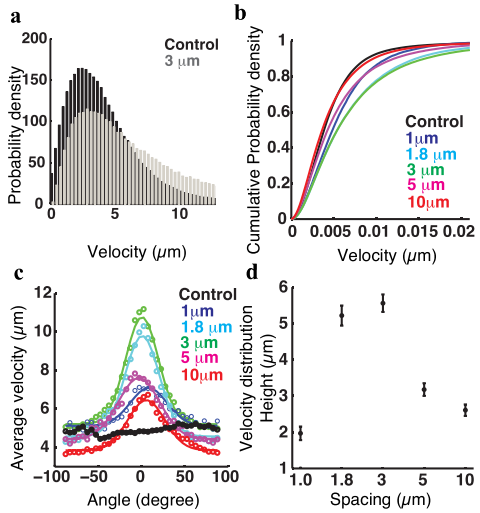

Figure 5. Velocity distribution of tracks depends on surface topography. (a) Frequency distribution of velocities for a flat control (black) and nanoridges with 3 μm spacing (green). (b) Cumulative distribution of velocities for all ridge spacings. Surfaces with 3 μm and 1.8 μm spacings show the highest velocities. (c) The distribution of velocity with respect to its angle to the ridge direction for all surfaces. Each point represents an average of all velocities within that range of angles. Binning was performed every 5°. The velocities exhibit a Gaussian distribution centered around zero angle. All distributions other than the control case were fit with a Gaussian distribution with a y offset. (d) Height of the velocity distribution obtained from the Gaussian fits in (c) as a function of ridge spacing.

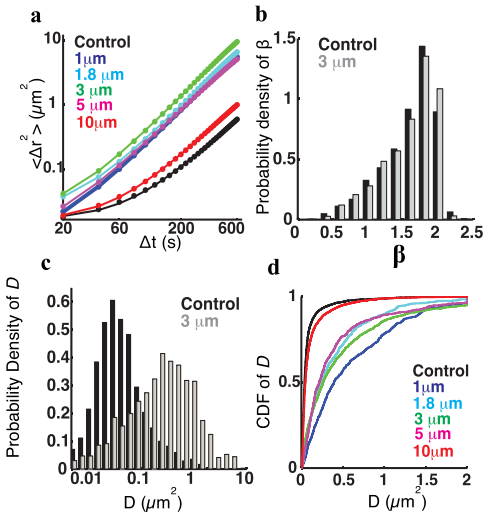

Figure 6. Micro/nanopatterns lead to superdiffusive motion of palladin bands. (a) Ensemble MSD as a function of time lag for all cells on surfaces with different ridge spacing. The MSD follows a power-law function, as described in methods. All best-fit lines have $R^2 > 0.9$. For all tracking experiments ~10 cells were analyzed for each ridge spacing, corresponding to ~1000–3000 individual tracks per spacing. (b) The probability density of the power-law exponent β for the flat control surface and for surfaces with 3 μm ridge spacing. (c) Probability density of the effective diffusion coefficient D for the flat control surface and for surfaces with 3 μm ridge spacing. (d) The cumulative probability distribution of D for the flat surface and different ridge spacings.

changeover occurs in approximately the first minute (figure 6(a)).

We next calculated the probability density of each fit parameter for tracks that exhibited a goodness-of-fit $R^2 > 0.9$. The distribution of the exponent β for these tracks showed a rightward skew that peaked around 1.8 and declined rapidly at 2 with less than 0.5% of all tracks exhibiting $\beta > 2.1$ (shown for the flat and 3 μm spacing surface in figure 6(b)). The effective diffusion coefficient, D, varied over a large range of values and followed a roughly log-normal distribution (figure 6(c)). Similar to ensemble average distributions, D was much larger for patterned surfaces than on a flat surface. The distribution of D for a 3 μm spacing surface was significantly shifted to the right, indicating higher D values than on a flat surface (figure 6(c)). The median of D for a 3 μm substrate was ~0.26 μm^2, whereas for a flat surface it was ~0.038 μm^2, almost 7 times smaller. The cumulative probability distribution of D for patterned surfaces also shows significant differences from that on a flat surface (figure 6(d)). Taken together these results indicate that the cell cytoskeleton shows a more dynamic behavior on ridges than on flat surfaces.

To further investigate the movement of palladin bands, we quantified the directionality of the tracks by plotting the probability distribution of the turning angle $\varphi(t, \Delta t)$ for $\Delta t = 120$ s [43]. We observed a peak in the turning angles at 0°, indicating persistent movement (figure 7(a)). We also examined the dependence

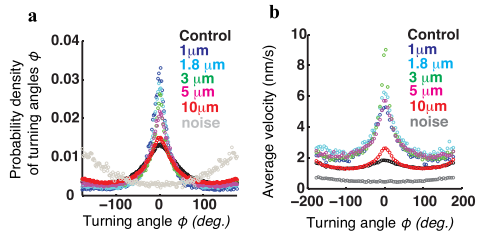

Figure 7. Palladin band diffusion on nanopatterns is temporally correlated. (a) The probability density of the turning angle $\varphi(t, \Delta t)$ for $\Delta t = 120$ s, which is peaked 0°. (b) The average velocity as function of the turning angle for $\Delta t = 120$ s, which is also peaked at 0°. Each point represents an average of all velocities within that range of angles. Binning was performed every 5°. The distribution shows a biphasic relationship of velocities, which peaks at 3 μm spacing. The different colors correspond to different ridge spacings and the grey line corresponds to noise.

of instantaneous velocities on the turning angles. We divided the range of all possible directions (from −90° to 90°) into 5° bins and averaged all velocities in a given angle bin. The resulting velocity distributions (figure 7(b)) for different surfaces as a function of angle showed a pronounced peak at 0° for all ridge spacings. These distributions exhibited a biphasic dependence on ridge spacing with highest average velocities for the 3 μm spacing surfaces, consistent with our results on biphasic dependence of other parameters.

Overall, our results indicate that in addition to cell shapes being aligned with nanotopographical features, the movement of intracellular cytoskeletal components is also strongly modulated with micro/nanotopography.

Discussion

In this study, we investigated the response of tumor-associated fibroblast cells to micro/nanotopography. We found that cell shape, focal adhesion and stress fiber alignment demonstrate a strong biphasic relationship between the degree of alignment and the spacing of ridges on the patterned substrates. Focal adhesions were preferentially distributed along the high curvature surfaces on the top of the nanoridges and were more likely to be aligned parallel to the nanoridges. Using EGFP-palladin as a marker, we analyzed the dynamics of stress fibers and their response to micro/nanotopography. Because ventral stress fibers originate at focal adhesions, the direction of focal adhesions can guide the direction of these stress fibers, which may explain the overall alignment of stress fibers, and hence cell shape, along the ridges. Our results are consistent with theories suggesting that overall cell alignment is induced by alignment of focal adhesions [25, 45], however focal adhesions alone do not explain the loss of mechanosensitivity for densely spaced patterns. Nanofabricated ridges may provide similar geometric constraints as collagen fibrils in connective tissue and the tumor microenvironment. Collagen fibrils have been measured to be between 100 and 500 nm wide and several microns long [8]. While the topography of real tissue is more complex, these nanofabricated ridges can potentially provide important insight into cellular responses to topography at the subcellular scale.

Although previous studies have shown that cell shape and movements align with nanotopographic patterns, the degree of this alignment appears to differ with cell type and pattern heights [12, 15, 40, 46]. A recent study has shown that surfaces with nanocraters repel cells, affecting focal adhesion formation and guiding cell migration [30]. While focal adhesion formation and cell migration on nanostructured surfaces has been studied, our study is one of the first to examine cytoskeletal dynamics on micro/nanopatterned surfaces. Our studies further indicate that topography sensing is optimal for surfaces with intermediate ridge spacings. It is intuitive that cells may lose their substrate sensitivity for ridged patterns with large spacing, as that approaches the topography of a flat surface. However, the loss of sensitivity on patterns with smaller ridge spacing is still somewhat puzzling. Previous studies [12, 15, 40, 46] have shown the loss of alignment of cells on both ends of the ridge spacing spectrum. However, due to technical limitations, ridges with a small spacing also had a smaller height. Thus, the loss of substrate sensitivity on patterns of smaller spacing could potentially come from the lower height of the ridges. Because the ridge height in our study did not vary with spacing, our results indicate that cells can lose their sensitivity on smaller spacing independent of ridge height. Finally, based on transcriptomic analysis of TAFs [55], we believe that TAF cells do not alter phenotype in response to micro/nanotopographic surfaces over the periods of time considered here, maintaining their fibroblast characteristics.

Our results show that stress fibers are more dynamic on micro/nanotopographic surfaces, with higher instantaneous velocities of palladin bands, which likely represent sarcomeric units, observed for all patterned surfaces compared with a flat surface. Stress fiber dynamics in cells arise from the elongation of stress fibers from focal adhesions, disassembly along the length of the fibers, and the contractile action of myosin motors which causes stress fibers to stretch and elongate or compress and leads to recruitment of cytoskeletal associated proteins such as zyxin and palladin [47–50]. A previous study [48] showed that palladin band movement was inhibited in the presence of actin polymerization inhibitors (cytochalasin), actin filament stabilizers (jasplakinolide) or myosin motor inhibitors (blebbistatin or Rho). Because prolonged application (10 min) of all these drugs resulted in stress fiber disassembly, we were unable to use these drugs to analyze stress fiber dynamics in our experiments, which required ~30 min of imaging.

Although on times scales from milliseconds to seconds, thermally driven motion can be relevant, the motion of the intracellular objects we observe are likely to result from myosin-based stress fluctuations of the cellular cytoskeleton [41, 42, 51], as evident from the superdiffusive motion of the palladin bands, both on flat and patterned surfaces. We observed that components within actin stress fibers undergo complex motion and exhibit regimes of subdiffusive and superdiffusive behavior on short and long time scales, respectively. The effective diffusion coefficient, D, is higher for all patterned surfaces as compared to flat surfaces, and peaks for ridges with 3 μm spacing. We note that the diffusive motion of the palladin bands can arise from two sources. Myosin contractility within the stress fiber accompanied by actin polymerization at the ends of the fiber leads to motion along the tangent vector of the stress fiber. In addition, the stress fiber is forced by myosin-driven contractions of the entire cytoskeletal network, leading to transverse motion of the stress fiber. Our observations of the peaked turning-angle distribution of the palladin puncta on patterned surfaces indicates that there is minimal transverse motion of the fibers, suggesting that the stress fiber network is stiffer on patterned surfaces, compared to flat surfaces.

Previous studies [48] have shown that the addition of a small amount of a phosphatase inhibitor, calyculin, leads to global dynamics and rearrangement of stress fibers by induction of myosin contractility. Our observations of enhanced dynamics of stress fibers imply that a purely geometric effect also has the potential to have a

direct influence on actin polymerization rates, myosin contractility, or both. This influence may be mediated by the preferential accumulation of curvature sensing proteins at the ridges, which can then stimulate actin nucleators and stimulate focal adhesion assembly, stress fiber formation and myosin activation [52, 53]. Overall, our observations imply that stress fiber growth dynamics and/or contractility are significantly enhanced on topographically patterned surfaces, suggesting that topography at the subcellular scale regulates cell contractility.

Based on our observations, we propose the following scenario for the non-monotonic effect of nature of stress fiber and focal adhesion alignment by micro/nanopatterns (supplementary figure 2). Previous studies have shown that cells spread anisotropically and exhibit non-monotonic stress fiber orientation as a function of substrate stiffness [54, 56]. A similar explanation may be at hand for the effect of topography on cell shape and stress fiber polarization. On flat surfaces, as the cell spreads, the tensile stress developed is essentially isotropic, resulting in isotropic polarization of stress fibers [54]. On patterned substrates, analysis of the cell shape as well the palladin bands shows that actin stress fibers prefer to move in the direction of ridges. Hence any misalignment of actin stress fibers with the ridges, could result in additional strain within the actin network, which can be relieved by regulating the spatial density of focal adhesions. On patterns with small spacing, the cell is able to nucleate increased numbers of focal adhesions in regions of higher stress fiber strain, which enables the cell to maintain its shape and accommodate the stress fibers that are misaligned. On substrates with larger spacing, longer focal adhesions are not capable of forming at high density. Since the nanoridges are too far away from each other and focal adhesions between the ridges are much smaller, a group of long focal adhesions formed on nanoridges allows for the anchoring of stress fibers forcing them to align with the ridges. We hypothesize that this occurs for the intermediate, 3 and 5 μm spaced ridges, where we observed the greatest degree of stress fiber alignment. Conversely, the largest spacing patterns of 10 μm provide space for FA to form between the ridges with more diverse angles with respect to the ridges (as we observe). This leads to a more normal cell morphology (less elongated, with SF less aligned). As the size between the ridges increases, it is expected that cells will have decreased interaction with ridges (since the area of overlap between cells and ridges becomes minimal), and cells will revert back to the 'flat' morphology, thus leading to the observed biphasic dependence on ridge spacing.

Overall, our results suggest that cellular mechanosensing of micro/nanotopography is highly dynamic in nature. We suggest that many factors, such as curvature sensing proteins and focal adhesions, which in turn affect actin polymerization, are sensitive to local geometry. These local responses in adhesion formation and maturation along with global coordination of the movement of actin stress fibers in the direction of imposed geometric constraints, could lead to large-scale alignment of the cell shape and its components with topographical cues. Sensing of micro/nanotopography is important for many cell types and may be particularly significant for TAFs, as these cells are constituents of the tumor microenvironment and therefore in constant interaction with ECM components such as collagen fibrils.

Acknowledgments

This work was supported by the National Science Foundation grant 1121710 and the NIH grant R21 AI122205. The authors thank Dr King Lam Hui for help with generation of the EGFP-palladin cell line.

References

[1] Bozec L, van der Heijden G and Horton M 2007 Collagen fibrils: nanoscale ropes *Biophys. J.* **92** 70–5
[2] Abrams G A, Goodman S L, Nealey P F, Franco M and Murphy C J 2000 Nanoscale topography of the basement membrane underlying the corneal epithelium of the rhesus macaque *Cell Tissue Res.* **299** 39–46
[3] Goodman S L, Sims P A and Albrecht R M 1996 Three-dimensional extracellular matrix textured biomaterials *Biomaterials* **17** 2087–95
[4] Amatangelo M D, Bassi D E, Klein-Szanto A J and Cukierman E 2005 Stroma-derived three-dimensional matrices are necessary and sufficient to promote desmoplastic differentiation of normal fibroblasts *Am. J. Pathol.* **167** 475–88
[5] Bellail A C, Hunter S B, Brat D J, Tan C and Van Meir E G 2004 Microregional extracellular matrix heterogeneity in brain modulates glioma cell invasion *Int. J. Biochem. Cell Biol.* **36** 1046–69
[6] Bettinger C J, Langer R and Borenstein J T 2009 Engineering substrate topography at the micro- and nanoscale to control cell function *Angew. Chem.* **48** 5406–15
[7] Curtis A and Wilkinson C 1997 Topographical control of cells *Biomaterials* **18** 1573–83
[8] Kim D H, Provenzano P P, Smith C L and Levchenko A 2012 Matrix nanotopography as a regulator of cell function *J. Cell Biol.* **197** 351–60
[9] Provenzano P P *et al* 2006 Collagen reorganization at the tumor-stromal interface facilitates local invasion *BMC Med.* **4** 38
[10] Provenzano P P, Inman D R, Eliceiri K W, Trier S M and Keely P J 2008 Contact guidance mediated three-dimensional cell migration is regulated by Rho/ROCK-dependent matrix reorganization *Biophys. J.* **95** 5374–84
[11] Berry C C, Campbell G, Spadiccino A, Robertson M and Curtis A S 2004 The influence of microscale topography on fibroblast attachment and motility *Biomaterials* **25** 5781–8
[12] Biela S A, Su Y, Spatz J P and Kemkemer R 2009 Different sensitivity of human endothelial cells, smooth muscle cells and fibroblasts to topography in the nano-micro range *Acta Biomater.* **5** 2460–6
[13] Driscoll M K, Sun X, Guven C, Fourkas J T and Losert W 2014 Cellular contact guidance through dynamic sensing of nanotopography *ACS Nano* **8** 3546–55
[14] Kaufmann D *et al* 2012 Partial blindness to submicron topography in NF1 haploinsufficient cultured fibroblasts indicates a new function of neurofibromin in regulation of mechanosensoric *Mol. Syndromol.* **3** 169–79
[15] Kim D H *et al* 2009 Mechanosensitivity of fibroblast cell shape and movement to anisotropic substratum topography gradients *Biomaterials* **30** 5433–44

[16] Sun X et al 2015 Asymmetric nanotopography biases cytoskeletal dynamics and promotes unidirectional cell guidance Proc. Natl Acad. Sci. USA 112 12557–62
[17] Brunetti V et al 2010 Neurons sense nanoscale roughness with nanometer sensitivity Proc. Natl Acad. Sci. USA 107 6264–9
[18] Sjostrom T et al 2009 Fabrication of pillar-like titania nanostructures on titanium and their interactions with human skeletal stem cells Acta Biomat. 5 1433–41
[19] Dalby M J et al 2007 The control of human mesenchymal cell differentiation using nanoscale symmetry and disorder Nat. Mater. 6 997–1003
[20] Oh S et al 2009 Stem cell fate dictated solely by altered nanotube dimension Proc. Natl Acad. Sci. USA 106 2130–5
[21] Bettinger C J, Zhang Z, Gerecht S, Borenstein J T and Langer R 2008 Enhancement of in vitro capillary tube formation by substrate nanotopography Adv. Mater. 20 99–103
[22] Dulgar-Tulloch A J, Bizios R and Siegel R W 2009 Human mesenchymal stem cell adhesion and proliferation in response to ceramic chemistry and nanoscale topography J. Biomed. Mater. Res. A 90 586–94
[23] Liliensiek S J, Campbell S, Nealey P F and Murphy C J 2006 The scale of substratum topographic features modulates proliferation of corneal epithelial cells and corneal fibroblasts J. Biomed. Mater. Res. A 79 185–92
[24] Liliensiek S J et al 2010 Modulation of human vascular endothelial cell behaviors by nanotopographic cues Biomaterials 31 5418–26
[25] Yim E K et al 2005 Nanopattern-induced changes in morphology and motility of smooth muscle cells Biomaterials 26 5405–13
[26] Lim J Y, Hansen J C, Siedlecki C A, Runt J and Donahue H J 2005 Human foetal osteoblastic cell response to polymer-demixed nanotopographic interfaces J. R. Soc. Interface 2 97–108
[27] Milner K R and Siedlecki C A 2007 Fibroblast response is enhanced by poly(L-lactic acid) nanotopography edge density and proximity Int. J. Nanomed. 2 201–11
[28] Milner K R and Siedlecki C A 2007 Submicron poly(L-lactic acid) pillars affect fibroblast adhesion and proliferation J. Biomed. Mater. Res. A 82 80–91
[29] Diehl K A, Foley J D, Nealey P F and Murphy C J 2005 Nanoscale topography modulates corneal epithelial cell migration J. Biomed. Mater. Res. A 75 603–11
[30] Jeon H et al 2015 Directing cell migration and organization via nanocrater-patterned cell-repellent interfaces Nat. Mater. 14 918–23
[31] Brammer K S, Oh S, Gallagher J O and Jin S 2008 Enhanced cellular mobility guided by TiO_2 nanotube surfaces Nano Lett. 8 786–93
[32] Ranucci C S abd Moghe P V 2001 Substrate microtopography can enhance cell adhesive and migratory responsiveness to matrix ligand density J. Biomed. Mater. Res. 54 149–61
[33] Teixeira A I, Abrams G A, Bertics P J, Murphy C J and Nealey P F 2003 Epithelial contact guidance on well-defined micro- and nanostructured substrates J. Cell Sci. 116 1881–92
[34] Hoon J L, Tan M H and Koh C G 2016 The regulation of cellular responses to mechanical cues by Rho GTPases Cells 5 17
[35] LaFratta C N, Fourkas J T, Baldacchini T and Farrer R A 2007 Multiphoton fabrication Angew. Chem. 46 6238–58
[36] Li L, Gattass R R, Gershgoren E, Hwang H and Fourkas J T 2009 Achieving lambda/20 resolution by one-color initiation and deactivation of polymerization Science 324 910–3
[37] Bayindir Z et al 2005 Polymer microcantilevers fabricated via multiphoton polymerization Appl. Phys. Lett. 86 064105
[38] Aguet F, Antonescu C N, Mettlen M, Schmid S L and Danuser G 2013 Advances in analysis of low signal-to-noise images link dynamin and AP2 to the functions of an endocytic checkpoint Dev. Cell 26 279–91
[39] Parast M M and Otey C A 2000 Characterization of palladin, a novel protein localized to stress fibers and cell adhesions J. Cell Biol. 150 643–56
[40] Lamers E et al 2010 The influence of nanoscale grooved substrates on osteoblast behavior and extracellular matrix deposition Biomaterials 31 3307–16
[41] Fakhri N et al 2014 High-resolution mapping of intracellular fluctuations using carbon nanotubes Science 344 1031–5
[42] Guo M et al 2014 Probing the stochastic, motor-driven properties of the cytoplasm using force spectrum microscopy Cell 158 822–32
[43] Raupach C et al 2007 Stress fluctuations and motion of cytoskeletal-bound markers Phys. Rev. E 76 011918
[44] Endlich N, Otey C A, Kriz W and Endlich K 2007 Movement of stress fibers away from focal adhesions identifies focal adhesions as sites of stress fiber assembly in stationary cells Cell Motil. Cytoskeleton 64 966–76
[45] Liang E I, Mah E J, Yee A F and Digman M A 2017 Correlation of focal adhesion assembly and disassembly with cell migration on nanotopography Integr. Biol. 9 145–55
[46] Lamers E et al 2010 The influence of nanoscale topographical cues on initial osteoblast morphology and migration Eur. Cells Mater. 20 329–43
[47] Hoffman L M, Jensen C C, Chaturvedi A, Yoshigi M and Beckerle M C 2012 Stretch-induced actin remodeling requires targeting of zyxin to stress fibers and recruitment of actin regulators Mol. Biol. Cell 23 1846–59
[48] Peterson L J et al 2004 Simultaneous stretching and contraction of stress fibers in vivo Mol. Biol. Cell 15 3497–508
[49] Smith M A et al 2013 LIM domains target actin regulators paxillin and zyxin to sites of stress fiber strain PloS One 8 e69378
[50] Yoshigi M, Hoffman L M, Jensen C C, Yost H J and Beckerle M C 2005 Mechanical force mobilizes zyxin from focal adhesions to actin filaments and regulates cytoskeletal reinforcement J. Cell Biol. 171 209–15
[51] Mizuno D, Tardin C, Schmidt C F and Mackintosh F C 2007 Nonequilibrium mechanics of active cytoskeletal networks Science 315 370–3
[52] Galic M et al 2012 External push and internal pull forces recruit curvature-sensing N-BAR domain proteins to the plasma membrane Nat. Cell Biol. 14 874–81
[53] Zhao H, Pykalainen A and Lappalainen P 2011 I-BAR domain proteins: linking actin and plasma membrane dynamics Curr. Opin. Cell Biol. 23 14–21
[54] Zemel A, Rehfeldt F, Brown A E, Discher D E and Safran S A 2010 Optimal matrix rigidity for stress fiber polarization in stem cells Nat. Phys. 6 468–73
[55] Cannon A R et al 2015 Palladin expression is a conserved characteristic of the desmoplastic tumor microenvironment and contributes to altered gene expression Cytoskeleton 72 402–11
[56] Azatov M, Goicoechea S M, Otey C A and Upadhyaya A 2016 The actin crosslinking protein palladin modulates force generation and mechanosensitivity of tumor associated fibroblasts Sci. Rep. 6 28805